ACS OMEGA

Open Access

http://pubs.acs.org/journal/acsodf

Article

Synthesis, Characterizations, Hirshfeld Surface Analysis, DFT, and NLO Study of a Schiff Base Derived from Trifluoromethyl Amine

Muhammad Nawaz Tahir, Muhammad Ashfaq, Khurram Shahzad Munawar, Ahsan Ullah Khan, Muhammad Adnan Asghar,* Tansir Ahamad, and Suvash Chandra Ojha*

Cite This: *ACS Omega* 2024, 9, 2325−2338

Read Online

ACCESS | Metrics & More | Article Recommendations | Supporting Information

ABSTRACT: We synthesized an imine-based (Schiff base) crystalline organic chromophore, i.e., (*E*)-2-ethoxy-6-(((3-(trifluoromethyl)phenyl)imino)methyl)phenol (**ETPMP**), and explored its nonlinear optical (NLO) properties. The crystalline structure of **ETPMP** was determined by the XRD technique and equated with the associated structures utilizing a Cambridge Structural Database search. The supramolecular assembly of **ETPMP** was investigated regarding intermolecular interactions and short contacts by Hirshfeld surface analysis. Void analysis was performed to check the mechanical response of the crystal. Supramolecular assembly was further inspected by interaction energy calculations that were performed with the B3LYP/6-31G(d,p) functional. Besides this, the NLO properties of **ETPMP** and other already reported crystal **TFMOS** were explored utilizing the M06/6-31G(d,p) functional of the DFT approach. An excellent agreement was observed between XRD and DFT results of geometric parameters of the above-mentioned crystals. Narrow band gap along with bathochromic shift (3.489 eV and 317.225 nm, respectively) were investigated in **TFMOS** than that of **ETPMP**. Owing to these unique properties, **TFMOS** possesses higher linear ($\langle a \rangle = 3.835 \times 10^{-23}$ esu) and nonlinear ($\gamma_{tot.} = 1.346 \times 10^{-34}$ esu) response as compared to **ETPMP**. The outcomes explicitly show the higher nonlinearity in **TFMOS**, highlighting its importance in potential NLO applications.

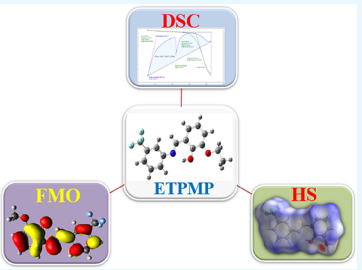

1. INTRODUCTION

There is an ongoing scientific interest in acquiring and studying Schiff bases since the very first synthetic report of these kinds of organic chemical compounds was documented in the middle of the 19th century.[1] A Schiff base may also be known as an azomethine or an imine compound. These substances are usually formed through the condensing aldehydes or ketones with the primary amines along with the exclusion of water molecules under some controlled reaction conditions in the alcoholic environment.[2] A Schiff base is a nitrogen counterpart of an aldehyde or ketone having an imine or azomethine group (−HC═N) added instead of the carbonyl group (C═O).[3]

The important therapeutic products with antimicrobial, antiproliferative, antipyretic, and antiviral characteristics are synthesized using Schiff bases as starting materials.[4] The −HC═N bond is necessary for biological action in azomethine derivatives.[5] These benefits, together with their higher stability and the wide range of structural forms they take, elucidate their importance as therapeutic drugs, with their aromatic and hydrophilic properties enhancing the biological impact.[6] They are also utilized in a broad variety of industrial practices, covering the fabrication of dyes, paints, and pigments.[7]

It is quite intriguing how a Schiff base chelates with transition metal ions. A Schiff base chelates with the metal ion via the nitrogen atom of the azomethine linkage. If a functional group that is close enough to −HC═N has a removable hydrogen atom, then it gives further stability to the metal complexes on chelation.[8] Moreover, almost all kinds of transition metals have a strong affinity for forming coordination compounds with the Schiff bases because of their smaller size and relatively higher nuclear charge.[9] Schiff bases derived from salicylaldehyde substituted with a halogen are well recognized for their effectiveness toward bacteria and fungi in terms of the structure−activity interaction.[10] Furthermore, it has been widely reported that the compounds including fluorine have garnered significant attention owing to their distinct physicochemical characteristics and biological action.[11]

The Schiff bases in which the hydroxyl (OH) group is present in close vicinity to the azomethine linkage show the process of tautomerism that is studied by utilizing various spectroscopic techniques and the SC-XRD method.[12] The Schiff bases in which the OH group is present ortho to −HC═N are of considerable interest owing to the presence of hydrogen bonding, which is due to tautomerism between the enol-imine and keto-amine forms. The stereochemical

Received: August 22, 2023
Revised: December 5, 2023
Accepted: December 15, 2023
Published: January 4, 2024

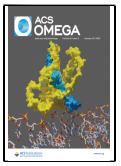

structure of these compounds results in shorter hydrogen bonds between the hydroxyl and the imino groups, as well as the imine nitrogen.[13] In rare cases, the imine nitrogen receives hydrogen from the OH group. In a nutshell, the balance between enol-imine and keto-amine goes mostly toward the direction of the keto-amine.[14]

A nonlinear optical behavior is present in many Schiff bases, which is based on the molecular units with additional electron donor and electron acceptor species on opposing ends of the molecule at suitable places on the aromatic ring to increase conjugation as well as significantly delocalize the π-electronic units.[15] Typically, several kinds of substituents with either electron-donating or electron-withdrawing groups are present in Schiff bases that are responsible for the nonlinear response.[16]

Based on the aforementioned applications, simple production, and numerous uses in NLO, Schiff bases are the most frequently utilized chemical compounds. Therefore, the appropriate synthesis and development of novel Schiff bases are extremely important. Hence, in continuation of our previous work,[17] we have synthesized a new Schiff base (**ETPMP**) by condensing 3-ethoxysalicylaldehyde with 3-(trifluoromethyl)aniline under an ethanolic environment. The Schiff base (**ETPMP**) was then characterized by SC-XRD, FTIR, UV−visible, and TGA/DSC techniques. Moreover, the computational analyses of **ETPMP** and a theoretically designed compound, i.e., **TFMOS**, have been conducted via density functional theory (DFT) as well as time-dependent density functional theory (TD-DFT) calculations. **TFMOS** has a close similarity with **ETPMP** because of its similar structure except for a carbonyl group instead of an alcoholic group at the ortho position and methoxy as the replacement of ethoxy at the meta position (see Figure S5 and optimized structures in Figure 1a) in **TFMOS**. Interestingly, the theoretically computed results of **ETPMP** have also been compared with the already reported similar synthesized compound, i.e., **TFMOS**[18] (different from **ETPMP** only due to the presence of methoxy instead of ethoxy at the meta position). We expect that this study will be beneficial for potential NLO applications in the future.

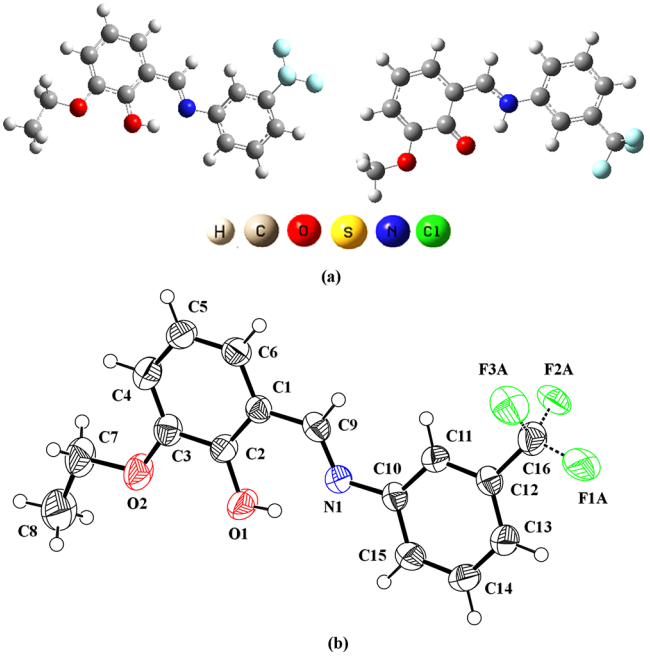

Figure 1. (a) The optimized structures of **ETPMP** and **TFMOS** and (b) ORTEP diagram of **ETPMP** drawn at the probability level of 50%. H atoms are shown by small circles of arbitrary radii. The main fragment of the disordered trifluoro assembly is shown for clarity.

2. EXPERIMENTAL SECTION

2.1. Material and Methods. The 2-hydroxy-3-ethoxybenzaldehyde, 3-(trifluoromethyl) aniline, and other analytical-grade reagents utilized in this investigation were acquired from Sigma-Aldrich. A Vario EL elemental analyzer was used for CHN analysis. The Gallen Kamp was employed to find out the melting point of the sample. The functional groups were sorted out using IRSpirit-T fitted with diamond ATR (Shimadzu) from 400 to 4000 cm^{-1}. TGA/DSC data were recorded utilizing a Discovery 650 SDT Simultaneous Thermal Analyzer. The data collection spanned from room temperature to 400 °C, and the instrument operated with a flow rate of 50 mL/min and a heating rate of 10 °C/min in a controlled environment consisting of 99.999% N_2 gas. DMSO was used as a solvent in the measurement of the absorption spectra using a CE 7200 double-beam UV−visible spectrophotometer. Pre-coated silica was used in thin-layer chromatography to track the progression of the chemical reaction and confirm the high purity of the resultant product.

2.2. Synthesis of (*E*)-2-Ethoxy-6-(((3-(trifluoromethyl)-phenyl)imino)methyl)phenol (ETPMP). A solution was prepared by dissolving 2-hydroxy-3-ethoxybenzaldehyde (1 mmol, 98%) in 30 mL of absolute EtOH within a 100 mL round-bottom flask followed by the dropwise addition of 3-(trifluoromethyl)aniline (1 mmol, ≥98%) through continuous stirring. Then, the contents were refluxed for 2−3 h. Upon verification of the completion of the reaction through TLC, the solution was subsequently cooled and shifted to a 100 mL beaker. The single crystals of **ETPMP** were obtained by the slow evaporation of that solvent that was suitable for XRD analysis (Scheme 1).

ETPMP: yield: 82%; M.P: 113 °C; color: brownish yellow; anal. calc. for $C_{16}H_{14}F_3NO_2$: C, 62.13; H, 4.56; N, 4.53; found: C, 62.16; H, 4.54; N, 4.55%; FTIR; 3049 (νC−H $_{aromatic}$), 2983 (νC−H $_{aliphatic}$), 1614 (νHC═N $_{azomethine}$), 1573 (νC═C $_{aromatic}$), 1153 (νC−N), 1106 (νC−F) (Figure S1); UV−vis; λ_{max} = 313 (π−π*) (Figure S2); TGA/DSC; 95% single step weight change between 133 and 220 °C, enthalpy (normalized); 2003 J/g, phase change at 113 °C; heat flow 1.518 W/g; residue 0%, peak temperature; 92.87 °C (Figure S3).

2.3. Single-Crystal XRD Structure Solution and Refinement Details. An appropriate single crystal was mounted on a Bruker Kappa Apex-II CCD diffractometer to collect X-ray data. The structural resolution and refinement were executed on SHELXT-2014[19] and SHELXL 2019/2,[20] respectively. Nonhydrogen atoms were assigned anisotropic displacement parameters, whereas hydrogen atoms were assigned isotropic displacement parameters. The H atoms were positioned at the calculated locations using a riding model. For making graphical illustrations of the results, ORTEP-III[21] and PLATON[22] software was used.

https://doi.org/10.1021/acsomega.3c05199
ACS Omega 2024, 9, 2325−2338

Scheme 1. Synthesis of ETPMP Using Substituted Aniline and Aldehyde

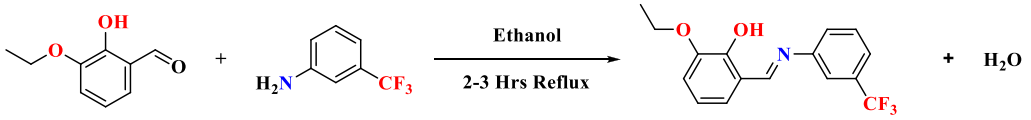

3. COMPUTATIONAL PROCEDURE

The theoretical investigation of the entire synthesized system (**ETPMP**) was done using the DFT and TD-DFT with M06[23] 6-31G(d,p) level approach. The experimental data of the said crystal was confirmed using the optimized geometrical analysis with the aid of SC-XRD and DFT approaches utilizing the Gaussian 09 program package.[24] The various software programs employed were Gaussview,[25] Gaussum,[26] Avogadro,[27] Chemcraft,[28] Multiwfn,[29] ArgusLab,[30] *etc.* The noncovalent interactions were analyzed via natural bond orbital (NBO) analysis using the NBO 5.0 program.[31] Moreover, NPA was performed to identify the atomic nature and bonding patterns of molecules with the help of Mulliken charges, and the molecular nature was verified accordingly. The crystallographic information files (CIFs) were utilized to further confirm the stabilities associated with optimized molecular geometries.

4. RESULTS AND DISCUSSION

4.1. Single-Crystal XRD and Supramolecular Assembly Inspection of ETPMP. In the compound **ETPMP** (Figure 1b, Table 1, and Table S14), the 2-ethoxy-6-methylphenol aldehyde group A (C1−C9/O1/O2) and *m*-toluidine group B (C10−C16/N1) of the aniline part are planar with root-mean-square (r.m.s.) deviations of 0.0131 and 0.0083 Å, respectively. Group A is oriented at the dihedral angle of 8.3 (9)° relative to group B. The trifluoro group is disordered over three sets of sites with an occupancy ratio of 0.45(2):0.35(2):0.202(19), so the overall occupancy of each fluorine atom is 1. The dihedral angle of the main fragment of the trifluoro group (F1A-F3A) with other parts is 6.6 (1) and 2.6 (2)°. The presence of the trifluoromethyl moiety causes the molecule to adopt a nonplanar conformation. The crystal structure adopts an enol tautomeric form with intramolecular O−H···N bonding, resulting in the generation of an S(6) H-bonded loop.[32] The molecules are connected in dimeric formations through C−H···O bonds, with the CH group originating from the trifluoromethyl-substituted phenyl ring and the O atom originating from the hydroxyl group (Figure 2,

Table 1. Experimental details of SC-XRD for ETPMP

crystal data	ETPMP
CCDC	2262734
chemical formula	$C_{16}H_{14}F_3NO_2$
M_r	309.40
crystal system, space group	monoclinic, $P2_1/n$
temperature (K)	296
a, *b*, *c* (Å)	12.5765 (12), 4.7874 (3), 24.0871 (18)
β (°)	94.464 (4)
V (Å^3)	1445.9 (2)
Z	4
radiation type	Mo Kα
μ (mm^{-1})	0.12
crystal size (mm)	0.30 × 0.16 × 0.14
data collection	
diffractometer	Bruker Kappa APEXII CCD
absorption correction	Multiscan (SADABS; Bruker, 2007)
no. of measured, independent, and observed [$I > 2\sigma(I)$] reflections	8609, 3036, 1557
R_{int}	0.059
$(\sin \theta/\lambda)_{max}$ (Å^{-1})	0.634
refinement	
$R[F^2 > 2\sigma(F^2)]$, $wR(F^2)$, S	0.054, 0.131, 0.97
no. of reflections	3036
no. of parameters	258
no. of restraints	127
H-atom treatment	H-atom parameters constrained
$\Delta\rho_{max}$, $\Delta\rho_{min}$ (e Å^{-3})	0.18, −0.15

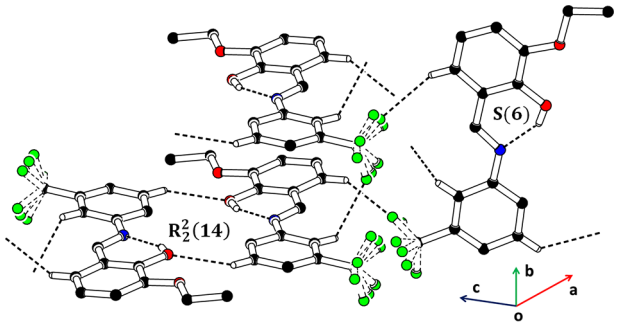

Figure 2. Packing diagram of **ETPMP** along with selected hydrogen atoms is depicted to enhance clarity.

Table 2. Hydrogen-Bond Geometry (Å, °) for ETPMP[a]

D—H···*A*	*D*—H	H···*A*	*D*···*A*	⟨(*D*—H···*A*)°
O1—H1···N1	0.82	1.86	2.589 (2)	147
C14—H14···O1^{i}	0.93	2.59	3.244 (3)	127
C11—H11···F2C^{ii}	0.93	2.55	3.08 (3)	117
C6—H6···F3A^{iii}	0.93	2.54	3.368 (13)	148

[a]Symmetry codes: (i) $-x + 1, -y + 1, -z + 1$; (ii) $x, y + 1, z$; (iii) $-x + 3/2, y + 1/2, -z + 1/2$.

Table 2). The O atom of the ethoxy group is not involved in any sort of H-bonding. The dimer is then further interlinked with two neighboring dimers by two C−H···F bondings. In one C−H···F bonding, the CH is from group A, whereas in another C−H···F bonding, the CH originates from group B. Within the crystal packing, there are very weak offset $\pi\cdots\pi$ stacking interactions observed. These interactions involve the separation between the centroids of the phenyl rings of symmetry-related molecules, which range from 4.5637 (15) to 5.2005 (14) Å. The Cambridge Structural Database search (CSD, 2023.2)[33] is employed to look for the closely related compounds from the literature. The crystal structures of (*E*)-2-methoxy-6-(((3-(trifluoromethyl)phenyl)imino)methyl)-

https://doi.org/10.1021/acsomega.3c05199
ACS Omega 2024, 9, 2325−2338

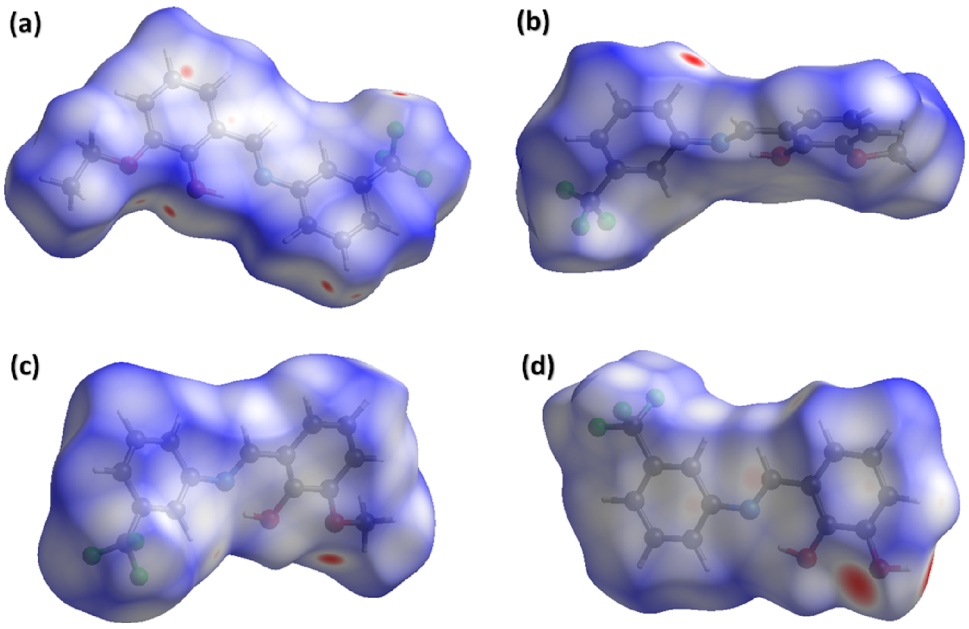

Figure 3. Hirshfeld surface plotted over d_{norm} for (a) **ETPMP** in the range from −0.0750 to 1.3433 a.u., (b) **TFMOS** in the range from −0.1752 to 1.3413 a.u. (first view), (c) **TFMOS** (second view), and (d) **TFHS** in the range from −0.6335 to 1.3643 a.u.

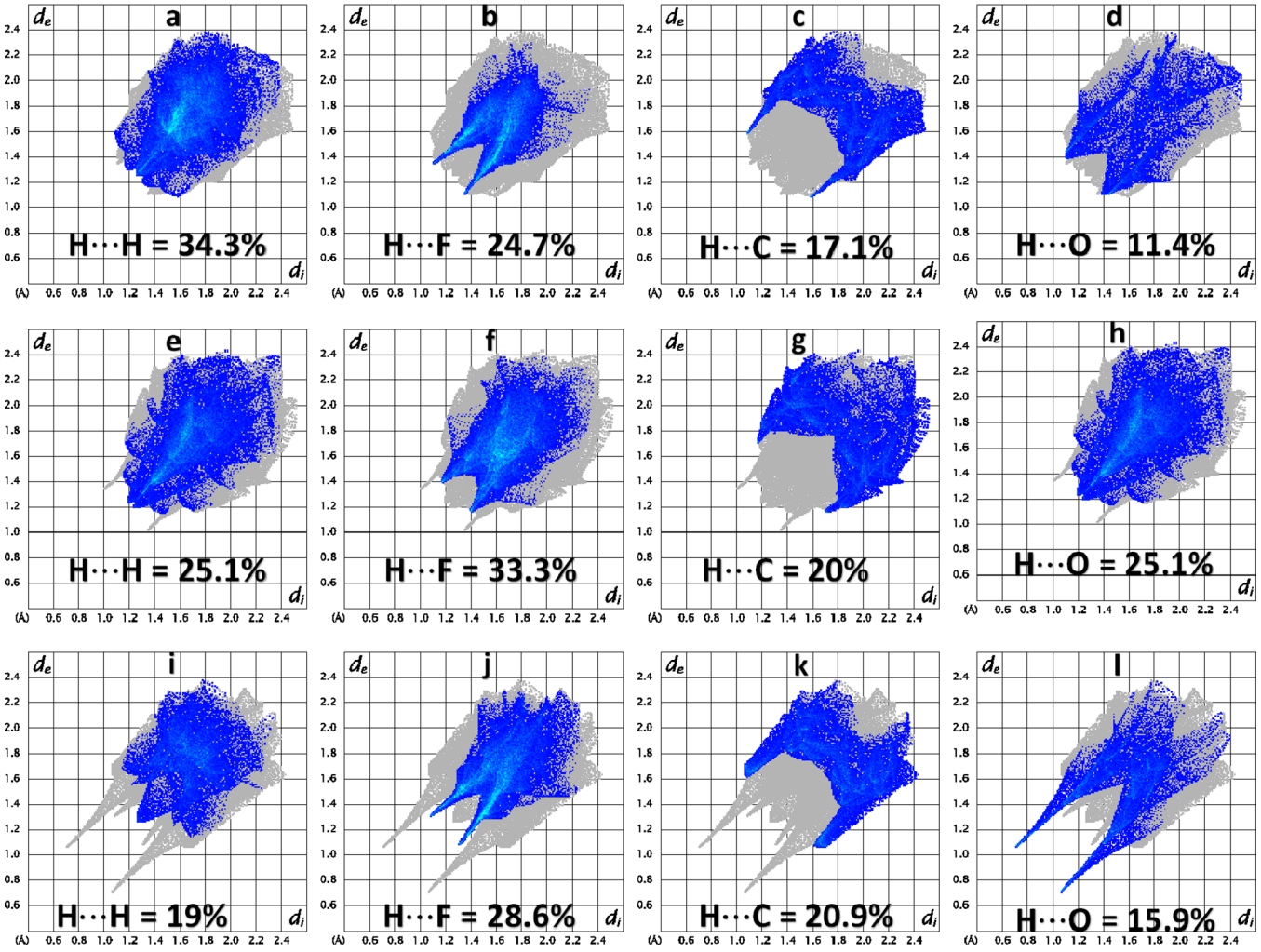

Figure 4. Important 2D plots for (a−d) **ETPMP**, (e−h) **TFMOS**, and (i−l) **TFHS**.

https://doi.org/10.1021/acsomega.3c05199
ACS Omega 2024, 9, 2325−2338

Table 3. Enrichment Ratio for the Pairs of Chemical Species in ETPMP, TFMOS, and TFHS[a]

	atom	H	C	N	O	F
contact %	H	34.3/25.1/19	17.1/20/20.9	0/1.3/0	11.4/11.1/15.9	24.7/33.3/28.6
	C	17.1/20/20.9	5.8/4.6/6.8	3.3/1.5/3.8	0.1/1.8/0.1	0.3/0.6/0.6
	N	0/1.3/0	3.3/1.5/3.8	0/0/0	0/0.1/0	0/0/0
	O	11.4/11.1/15.9	0.1/1.8/0.1	0/0.1/0	0/0/0	0/0.6/0
	F	24.7/33.3/28.6	0.3/0.6/0.6	0/0/0	0/0.6/0	3/0/4.3
surface %		60.9/57.95/51.7	16.2/16.55/19.5	1.65/1.45/1.9	5.75/6.8/8	15.5/17.25/18.9
random contacts %	atom	H	C	N	O	F
	H	37.09/33.58/26.73				
	C	19.73/19.8/20.16	2.62/2.74/3.80			
	N	2.01/1.68/1.96	0.53/0.48/0.74	0.03/0.02/0.04		
	O	7.00/7.88/8.27	1.86/2.25/3.12	0.19/0.20/0.30	0.33/0.46/0.64	
	F	18.88/19.99/19.54	5.02/5.71/7.37	0.51/0.50/0.72	1.78/2.35/3.02	2.40/2.98/3.57
enrichment ratio	atom	H	C	N	O	F
	H	0.92/0.75/0.71				
	C	0.87/1.04/1.04	2.21/1.68/1.79			
	N	0/0.77/0				
	O	1.63/1.41/1.92	0.05/0.80/0.03			
	F	1.31/1.67/1.46	0.06/0.11/0.08		0/0.26/0	1.25/0/1.20

[a]The enrichment ratio for pairs with random contacts less than 0.9 is not calculated.

phenol (**TFMOS**)[18] 3-(3-(trifluoromethyl)-phenyliminomethyl)benzene-1,2-diol (**TFHS**),[34] and (*E*)-2-methyl-6-(3-(trifluoromethyl)phenyliminomethyl)phenol (**TFMS**)[35] are reported in the literature that are relevant to **ETPMP**. The bond lengths and angles of **ETPMP** are consistent with the values found in the reported structures. The crystal packing of **ETPMP** has a close resemblance to that of **TFMOS** with one significant difference; that is, the $\pi\cdots\pi$ stacking interactions in **TFMOS** are stronger than in **ETPMP**. The crystal packing of **TFHS** was principally stabilized by O−HO bonding due to the presence of the hydroxyl group at the meta position, whereas for **TFMS**, the C−H$\cdots\pi$ and $\pi\cdots\pi$ stacking interactions were the packing stabilizers with no intermolecular H-bonding.

4.2. Hirshfeld Surface Analysis. For the researchers performing experiments on single crystals, it is really important to know the interactions that are the stabilizers of the supramolecular assembly.[36] The intermolecular interactions are the deciders of the properties of the crystal. To understand the dispersal of electron density within the molecules and the interaction of the molecule with its neighboring molecules, Hirshfeld surface analysis is executed on Crystal Explorer version 21.5.[37] To make that part of the manuscript interesting for the readers, the analysis of **ETPMP** is compared with two literature structures with reference codes **TFMOS** and **TFHS**. The Hirshfeld surface over d_{norm} is the key indicator of separating shorter contacts from longer contacts.[38] The surface has three colors: red for short contacts, blue for long contacts, and white for the contacts with a distance equal to the sum of van der Waals radii. Figure 3 is the Hirshfeld surface over d_{norm} for **ETPMP**, **TFMOS**, and **TFHS**. The red patches around the particular atoms on the surface showed that these atoms form short contacts. The hydroxyl group behavior to form short contact is different in **ETPMP**, **TFMOS**, and **TFHS**. In **ETPMP**, the hydroxyl moiety forms a short contact and acts as an H-bond acceptor, whereas in **TFMOS**, the hydroxyl is not involved in the H-bonding (Figure 3b,c). In **TFHS**, the hydroxyl group forms two short contacts; in one contact, it acts as an H-bond donor, whereas in the other contact, it behaves as an H-bond acceptor. In **TFMOS** and **TFHS**, the O atom of the group present at the para position is concerned with H-bonding, whereas in **ETPMP**, the corresponding O atom does not form an H-bond; although a light red spot is present around the O atom (Figure 3a), the contact is not short enough to form an H-bond.

Two-dimensional fingerprint plots break the crystal packing into smaller parts and contribute the contacts in the stabilization of the crystal packing. The important parameters in the 2D fingerprint plots are d_i and d_e. The important 2D plots of **ETPMP**, **TFMOS**, and **TFHS** are depicted in Figure 4a−d, e−h, and i−k, respectively. In the compounds mentioned above, C−H···O and C−H···F interactions are the primary intermolecular interactions. The predominant contacts involve H···C, H···F, and H···O, along with H···H interactions, as these compounds possess a considerable number of hydrogen atoms in comparison to other atom types. The H···H contact has the most substantial contribution in the supramolecular assembly of **ETPMP**, whereas for **TFMOS** and **TFHS**, the H···F contact is the most important one. The 2D plot of the H···O contact for **TFHS** has larger spikes as compared to the 2D plots of **ETPMP** and **TFMOS** that show that the H···O contact is stronger/shorter in **TFHS** as compared to those in **ETPMP** and **TFMOS**.

The enrichment ratio reflects the propensity of a pair of chemical species to engage in crystal-packing interactions. The enrichment ratio is greater than 1 for favorable contacts (contacts that are likely to form short contacts) and less than 1 for nonfavorable contacts. The most favorable contact is C···C in **ETPMP** and **TFMOS** with enrichment ratios of 2.21 and 1.68, respectively. For **TFHS**, the most favorable contact is H···O with an enrichment ratio of 1.92. The F···F contact is favorable in **ETPMP** and **TFHS** but not favorable in **TFMOS**. The H···H contact is not favorable in **ETPMP**, **TFMOS,** and **TFHS**. The H···C contact is equally favorable in **TFMOS** and **TFHS** but not favorable in **ETPMP** (Table 3).

4.3. Void Analysis. Voids in the crystal decide the mechanical response by the application of some external force. A crystal with larger cavities has a poor mechanical response. To predict the mechanical response of **ETPMP**, voids are calculated for **ETPMP** and compared with voids in

https://doi.org/10.1021/acsomega.3c05199
ACS Omega 2024, 9, 2325−2338

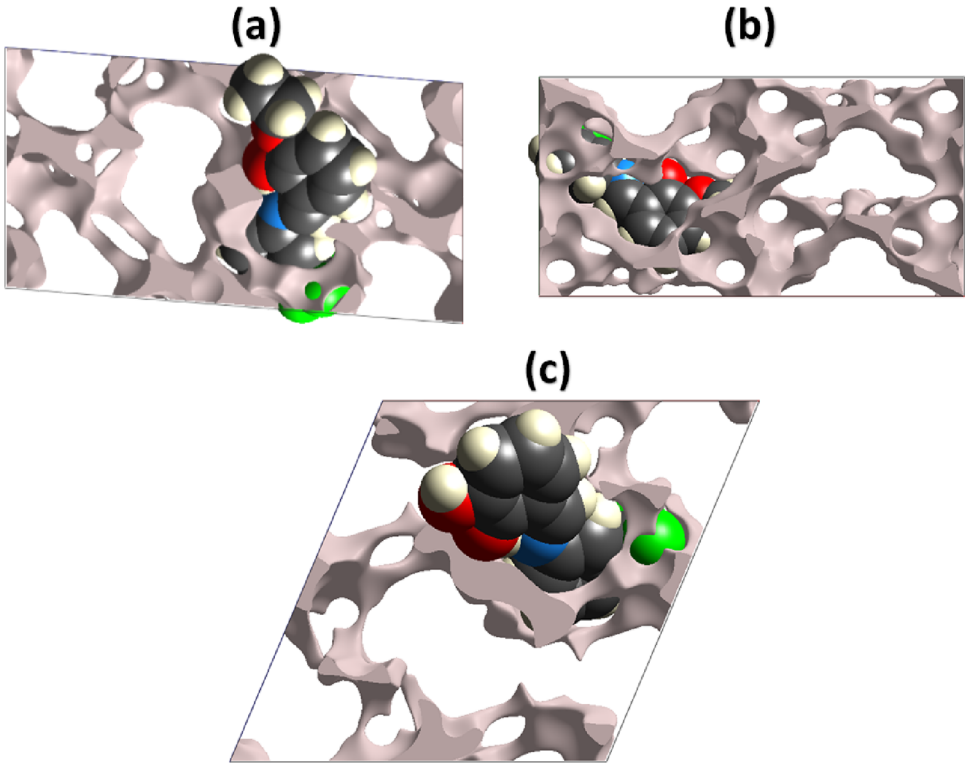

Figure 5. Graphical representation of (a) **ETPMP**, (b) **TFMOS**, and (c) **TFHS**.

TFMOS and **TFHS**. Voids are computed by adding up the electron density of all the atoms that are supposed to be spherically symmetric.[39] Voids for **ETPMP**, **TFMOS**, and **TFHS** are shown in Figure 5a−c, respectively. The volume of voids in **ETPMP**, **TFMOS**, and **TFHS** is calculated as 190.78, 405.20, and 133.85 $Å^3$, respectively. The voids occupy 13.2, 14.7, and 11.1% in **ETPMP**, **TFMOS,** and **TFHS**, respectively. The voids within the crystal packing occupy only a minimal amount of space, indicating the absence of significant cavities and suggesting a favorable mechanical response.

4.4. Interaction Energy and Energy Framework Investigation. For further inspection of the supramolecular assembly or crystal packing, the interaction energy is calculated for the molecular pairs in **ETPMP** and compared with the interaction energies in **TFMOS** and **TFHS**. For the calculations of interaction energies between molecular pairs, the B3LYP/6-31G(d,p) electron density model is used in Crystal Explorer version 21.5. A cluster of 3.8 Å is created around the molecule found in the asymmetric unit, and the interaction energies are subsequently computed among the molecules within this cluster. There are four types of interaction energy: electrostatic Coulomb, dispersion, polarization, and repulsion. In molecular interactions, both dispersion and polarization energies between pairs of molecules are consistently attractive, whereas repulsion energy is consistently repulsive. However, electrostatic Coulomb energy can either be attractive or repulsive. For crystals, dispersion and electrostatic Coulomb energies dominate over the other kinds of energies. The results of the interaction energy are presented in Tables S1 and S3 for **ETPMP**, **TFMOS**, and **TFHS**, respectively. In the case of molecular pairs within ETPMP and TFHS, the electrostatic Coulomb energy is attractive. However, for TFMOS, the electrostatic Coulomb energy is attractive for all pairs except those with intermolecular distances of 13.86, 10.42, 7.51, and 16.26 Å, where it exhibits a repulsive behavior. The greatest Coulomb energies are −20.7, −15.5, and −38.6 kJ/mol for **ETPMP**, **TFMOS**, and **TFHS**, respectively. The greatest dispersion energies are −78.0, −64.6, and −76.5 kJ/mol for **ETPMP**, **TFMOS,** and **TFHS**, respectively. An important result of the interaction energy calculations is that the largest total energy between the molecular pair does not have the same value for **ETPMP**, **TFMOS,** and **TFHS**. The largest total energy is −56.5, −51.7, and −54.5 kJ/mol for **ETPMP**, **TFMOS**, and **TFHS**, respectively. To check which energy is the most prominent donor to the crystal packing, energy frameworks are constructed (Figure S6). In **ETPMP**, **TFMOS**, and **TFHS**, a representation is created by connecting the centers of molecules with cylinders, and the width of these cylinders is directly proportional to the strength of the interaction energy. Notably, for these compounds, the widths of the cylinders representing the dispersion energy frameworks are greater than the widths of the cylinders for the Coulomb energy frameworks. Energy frameworks clearly show that the dispersion energy is the prominent contributor to the crystal packing in **ETPMP**, **TFMOS**, and **TFHS**.

4.5. FTIR Spectral Data. Infrared spectral studies serve as a powerful tool for identifying and characterizing the functional groups present in organic compounds. The most crucial peak in the FTIR spectral analysis, which serves as the strongest evidence of product formation, is the appearance of a characteristic band at 1614 cm^{-1} in **ETPMP**. This band is associated with the stretching vibrations of the azomethine linkage (HC═N), confirming the successful reaction of both precursors to yield the product. The absorption peak for aromatic C−H bonds appears at 3049 cm^{-1}, whereas aliphatic C−H bonds show their presence by displaying a peak at 2983 cm^{-1}. Two sharp peaks at 1573 and 1467 cm^{-1} are due to the

https://doi.org/10.1021/acsomega.3c05199
ACS Omega 2024, 9, 2325−2338

presence of the aromatic C=C stretching mode of vibrations. In addition to this, there are two prominent peaks observed at 1153 and 1106 cm^{-1}, which can be ascribed to the stretching vibrations of C−N and C−F, respectively. The sharp peak observed at 733 cm^{-1} corresponds to the out-of-plane bending vibrations of aromatic C−H bonds, whereas the in-plane aromatic C−H bending vibrations were identified at 1063 cm^{-1}.

4.5.1. Electronic Absorption Spectrum. The UV−vis spectrum of **ETPMP** was documented by using DMSO as a solvent. The spectrum exhibits only one broad absorption band at λ_{max} = 313 nm, which is ascribed to the n-π^* electronic transitions because of a lone pair on the sp^2 hybridized nitrogen of the azomethine linkage.

4.6. TGA/DSC Analysis. The TGA curve of **ETPMP** shows that it is stable up to 133 °C and then decomposes in a single step starting from 133 °C and ending up to 220 °C, showing a midpoint at 182 °C with almost 97% weight loss due to the degradation of all organic frameworks from the molecular structure. It is believed that **ETPMP** is pure because its DSC thermogram showed a single strong peak at 113 °C with a heat flow of 1.518 W/g, which is ascribed to endothermic melting or a phase change from solid to liquid.

5. COMPUTATIONAL STUDY

5.1. Geometric Parameters. The geometric parameters of **ETPMP** and **TFMOS** were evaluated using DFT calculations at the M06/6-31g (d,p) level of theory and basis set. A comparison between XRD and DFT-based results of these parameters is tabulated in Tables S6−S9, whereas Figure S4 displays the comparative statistical analysis in the form of column graphs for **ETPMP** and **TFMOS**, respectively. In **ETPMP**, the bond lengths of F1−C22, F2−C22, and F3−C22 were calculated as 1.336, 1.339, and 1.34 Å through DFT and 1.334, 1.343, and 1.321 Å through XRD, respectively. In compound **TFMOS**, the bond lengths of F1−C21, F2−C21, and F3−C21 were calculated as 1.339, 1.335, and 1.339 Å *via* DFT and 1.343, 1.369, and 1.304 Å *via* XRD, respectively. In **ETPMP**, the O−C bond lengths were found to be 1.33, 1.351, and 1.414 Å for O4−C8, O5−C9, and O5−C13, which strongly support XRD values 1.344, 1.367, and 1.426 Å. The oxygen−carbon bond lengths in **TFMOS** were calculated as 1.248, 1.349, and 1.403 Å through DFT and 1.357, 1.372, and 1.421 Å through XRD for O4−C8, O5−C9, and O5−C13, respectively. In **ETPMP**, the bond lengths for N6−C15 and N6−C16 were noted as 1.288 and 1.401 Å through DFT, which showed good agreement with XRD bond lengths, i.e., 1.285 and 1.41 Å. In **TFMOS,** nitrogen−carbon bond lengths for N6−C14 and N6−C15 are observed as 1.336 and 1.397 Å through DFT and 1.277 and 1.425 Å via XRD, respectively.

C−C bond lengths investigated in the case of **ETPMP** from the DFT approach are examined as 1.409, 1.409, 1.443, 1.416, 1.386, 1.403, 1.374, 1.506, 1.396, 1.4, 1.391, 1.389, 1.498, 1.392, and 1.385 Å for C1−C2, C1−C6, C1−C9, C2−C3, C3−C4, C4−C5, C5−C6, C7−C8, C10−C11, C10−C15, C11−C12, C12−C13, C12−C16, C13−C14, and C14−C15, respectively. Meanwhile, 1.395, 1.402, 1.441, 1.399, 1.379, 1.387, 1.365, 1.496, 1.386, 1.385, 1.381, 1.379, 1.489, 1.383, and 1.37 Å values were calculated by the XRD study. The carbon−carbon bond distances in **TFMOS** calculated through the DFT method were found to be 1.461, 1.432, 1.384, 1.462, 1.366, 1.43, 1.356, 1.398, 1.396, 1.385, 1.394, 1.499, 1.387, and 1.389 Å for C1−C2, C1−C6, C1−C8, C2−C3, C3−C4, C4−C5, C5−C6, C9−C10, C9−C214, C10−C11, C11−C12, C11−C15, C12−C13, and C13−C14, respectively, which showed great correlation with XRD results, i.e., 1.403, 1.402, 1.454, 1.413, 1.379, 1.378, 1.381, 1.387, 1.384, 1.392, 1.385, 1.49, 1.379, and 1.386 Å, respectively.

In **ETPMP**, the calculated bond angles for F1−C16−F2, F1−C16−F3, F1−C16−C18, F2−C16−F3, F2−C16−C18, and F3−C16- C18 observed as 107.4, 107.6, 112.4, 106.6, 111.3, and 111.3° in the case of DFT were found to be comparable with XRD data of 103.5, 106.9, 114.5, 105.6, 110.4, and 114.9°, respectively. When considering bond angles in the crystal compound **TFMOS**, those for F1−C15−F2, F1−C15−F3, F1−C15−C11, F2−C15−F3, F2−C15−C11, and F3−C15−C11 were obtained as 107.7, 106.7, 111, 107.6, 112.5, and 111.1° (via DFT) and 102.8, 107.3, 110.5, 106, 114.3, and 115° (via XRD), respectively.

The various bond angles between C−O atoms in **ETPMP** range from 107.4 to 125.4° when studied by DFT and found to be in good agreement with practical values measured through XRD (107−125.3°). In **TFMOS**, bond angles between different C−O atoms like the C−O atoms O1−C2−C1, O1−C2−C3, C3−O2−C7, O2−C3−C2, O2−C3−C4, O1−C2−C1, O1−C2−C3, C3−O2−C7, and O2−C3−C2 were calculated by DFT as 123.1, 121.3, 117.1, 113.1, 125.8, 123.1, 121.3, 117.1, and 113.1°. The above-mentioned results were also calculated through XRD as 122, 118.3, 117.7, 115.3, 125.6, 122, 118.3, 117.7, and 115.3°, respectively. C−N bond angles in **ETPMP** were observed as 120, 123.3, 122.7, and 118.2° (DFT) and 122.3, 122.3, 122.5, and 116.5° (XRD) for C9−N1−C10, N1−C9−C1, N1−C10−C11, and N1−C10−C15, respectively. In the same manner, the bond angles including C and N atoms of **TFMOS** like C8−N1−C9, N1−C8−C1, N1−C9−C10, and N1−C9−C14 were observed as 127.3, 123.7, 117.6, and 122.9° (DFT) and 120, 123.1, 117.4, and 122.5° (XRD), respectively.

In **ETPMP**, DFT calculated bond angles for different C−C atoms range (119−121.1°) in entitled compound, which are in accordance with the corresponding XRD results range (118.2−121.3°), respectively (see Tables S6 and Table S7). The comparative analysis of calculated molecular geometric parameters in DFT and XRD are correlated, except for a certain deviance, C−C bond angles in **TFMOS** range from 115.6 to 121° (DFT) for C2−C1−C6, C2−C1−C8, C1−C2−C3, C4−C5−C6, C10−C9−C14, C9−C10−C11, C9−C14−C13, C10−C11−C12, C10−C11−C15, C12−C11−C15, C11−C12−C13, and C12−C13−C24, which are closer to the corresponding XRD result range of 115.3−122°, respectively (Tables S8 and S9). The comparison between XRD and DFT values of bond length and bond angles of **TFMOS** and **ETPMP** are provided in Figures S7−S10. The RMSE of studied compounds is shown in the Supporting Information (Table S15)

5.2. Electronic Structure. Frontier molecular analysis is an eminent approach to explore the charge transfer possibility, chemical solidity, absorption spectra, and optoelectronic properties of molecules.[40,41] FMOs involve two molecular orbitals, i.e., the electron donating recognized as the HOMO and electron accepting known as the LOMO, which reveal the energy gap values between them.[42] The quantum orbital energy gap (E_{LUMO}−E_{HOMO}) elucidates the chemical parameters, i.e., softness, hardness, chemical reactivity, and chemical stability, of the investigated compound. Molecules with large HUMO−LUMO band gap are observed to be hard,

https://doi.org/10.1021/acsomega.3c05199
ACS Omega 2024, 9, 2325−2338

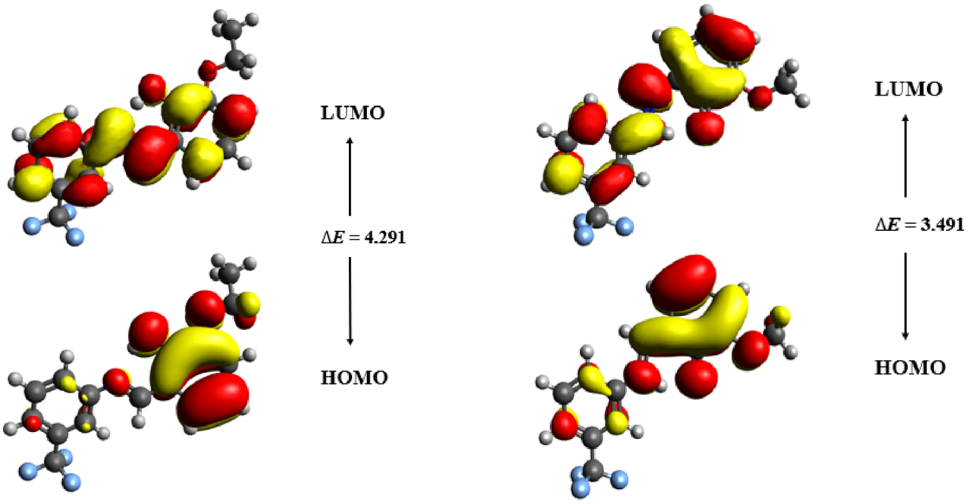

Figure 6. HOMOs and LUMOs of studied compounds **ETPM** and **MTPM**.

dynamically stable, and less reactive.[43] Less energy gap enhances the hyperpolarizability factor of a compound due to enhanced internal charge transmission.[44] So, when the energy gap between FMOs is lower, the molecule will be softer, more highly reactive, and hence more polarizable and subsequently act as the dominant NLO candidate.[45]

Table S13 displays the calculated energies for HOMO and LUMO for compounds **ETPM** and **MTPM**. In **ETPM**, HOMO corresponds to −5.972 eV, whereas LUMO possesses −1.681 eV of energy, with an energy gap between HOMO and LUMO of 4.291 eV. Similarly, computed HOMO and LUMO energy values for compound **MTPM** is observed at −5.476 and −1.985 eV, respectively, with a band gap value of 3.491 eV.

FMO surface diagrams are used to discover the internal charge transfer across the molecule. In **ETPM**, electronic density over the HOMO orbital is present across all the molecules except (trifluoromethyl) benzene, whereas for LUMO, charge density is present across the whole structure. Similarly, HOMO of **MTPM** contains electronic density that majorly lies upon (trifluoromethyl) benzene, and in LUMO, it is spread across the entire structure (Figure 6). The energies of HOMO − 1/LUMO + 1 and HOMO − 2/LUMO + 2 orbitals of both crystals are displayed in Table S13, whereas surface diagrams are presented in Figure S11.

5.3. Global Reactivity Parameters (GRPs). The band gap of HOMO/LUMO is used to understand the GRPs such as electronegativity (X),[46] ionization potential (IP),[47] electron affinity (EA),[48] chemical potential (μ),[49] global hardness (η),[50] global softness (σ),[51] and global electrophilicity index (ω).[52] Equations 1 and 2 are used to calculate IP and EA.

$$\mathrm{IP} = -E_{\mathrm{HOMO}} \tag{1}$$

$$\mathrm{EA} = -E_{\mathrm{LUMO}} \tag{2}$$

The η, X, and μ were determined by the help of Koopmans's theorem[53,54] utilizing eqs 3−5.

$$X = \mathrm{IP} + \mathrm{EA} \tag{3}$$

$$\eta = \mathrm{IP} - \mathrm{EA} \tag{4}$$

$$\mu = \frac{E_{\mathrm{LUMO}} + E_{\mathrm{HOMO}}}{2} \tag{5}$$

The σ is described by eq 6.

$$\sigma = \frac{1}{\eta} \tag{6}$$

Parr et al. introduced the ω from eq 7.

$$\omega = \frac{\mu^2}{2\eta} \tag{7}$$

Table 4 represents all the global reactivity descriptors for **ETPMP** and **TFMOS** calculated with the help of their

Table 4. Global Reactivity Descriptors of TFMOS and ETPMP in eV Whereas σ Is in eV^{-1}

parameter	ETPMP	TFMOS
IP	0.2195	0.2013
EA	0.0614	0.0732
X	0.1405	0.1373
μ	0.1581	0.1281
M	−0.1405	−0.1373
ω	0.1248	0.1471
σ	6.3251	7.8064

HOMO−LUMO band gaps. IP is defined as the energy required by HOMO to donate electrons, whereas EA is related to the ability of LUMO to attract electrons. μ is known as the energy per mole of a substance, which aids in understanding the chemical reactivity and stability of the studied chromophores. It is directly related to the stability of a molecule and varies inversely with the reactivity. **ETPMP** and **TFMOS** are donor−acceptor based configurations, and both exhibit higher values of IP with lower EA values, which represent the strong nature of donor moieties. Further, X, IP, and EA are also studied in relation to the E_{gap} of the synthesized crystal molecules. The electronegativity represents the electron-withdrawing ability of a chemical species. Among the studied chromophores, **TFMOS** is denoted as the softer compound, which possesses a higher global softness value of 7.8064 eV^{-1} compared to **ETPMP** with a calculated value of 6.3251 eV^{-1}. Contrarily, the global hardness (η) of **ETPMP** is greater than **TFMOS** (0.1581 〉 0.1281 eV), which is in

https://doi.org/10.1021/acsomega.3c05199
ACS Omega 2024, 9, 2325−2338

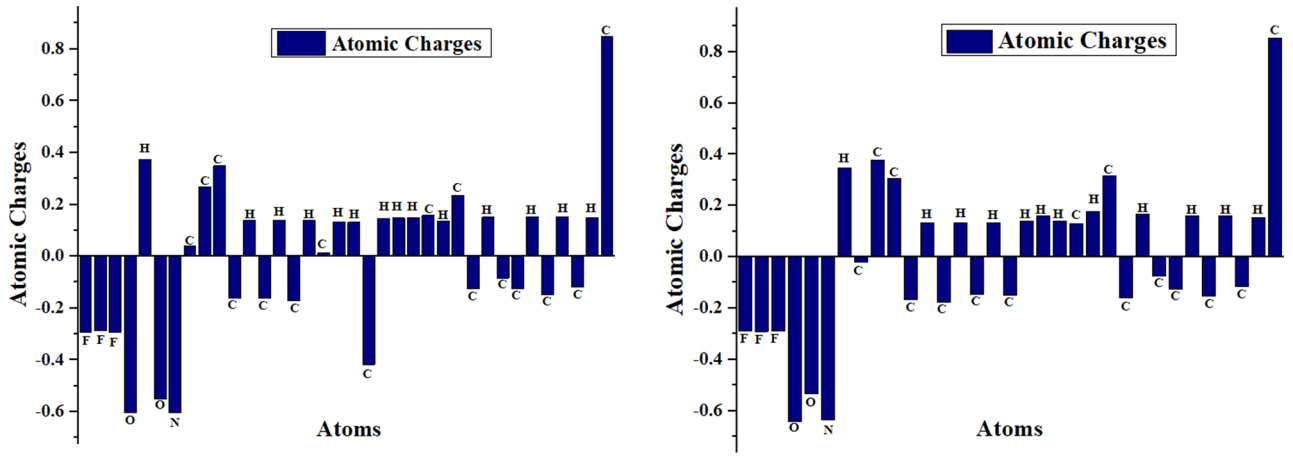

Figure 7. Natural population analysis of **ETPMP** and **TFMOS**.

Table 5. Representative Values of Natural Bond Orbital Analysis for ETPMP and TFMOS by Using the M06/6-31G (d,p) Level

compounds	donor (*i*)	type	acceptor (*j*)	type	$E^{(2)a}$	$E(j) - E(i)^b$ (a.u.)	$F(i,j)^c$ (a.u.)
ETPMP	C26−C27	Π	C29−C30	π^*	23.21	0.3	0.074
	C8−C9	Π	N7−C24	π^*	22.64	0.29	0.076
	C8−C9	Π	C8−C9	π^*	1.74	0.29	0.02
	O4−H5	Σ	C9−C10	σ^*	5.73	1.31	0.078
	C17−C20	Σ	C20−H23	σ^*	0.5	1.07	0.021
	O4	LP(2)	C8−C9	π^*	39.35	0.35	0.113
	F3	LP(2)	C29−C30	π^*	0.53	0.48	0.016
TFSMOS	N6−C23	Π	C8−C21	π^*	38.73	0.37	0.108
	C8−C21	Π	O4−C9	π^*	32.77	0.29	0.088
	N6−C23	Π	N6−C23	π^*	1.01	0.3	0.018
	C11−C13	Σ	O5−C10	σ^*	5.51	1.08	0.069
	C24−C26	Σ	F3−C33	σ^*	0.52	0.98	0.021
	C31	LP(1)	N6−C23	π^*	299.5	0.07	0.137
	F1	LP(1)	C26−C33	σ^*	0.54	1.48	0.026

[a]Energy of hyper conjugative interaction (stabilization energy), unit in kJ mol^{-1} (a.u.). [b]Energy difference between donor and acceptor *i* and *j* NBO orbital. [c]Fock matrix element between *i* and *j* NBO orbital.

accordance with their energy gap values, i.e., **TFMOS** with 3.489 eV and **ETPMP** with 4.300 eV. Moreover, a comparative analysis of **ETPMP** and **TFMOS** revealed that **ETPMP** is much softer (6.3251 eV^{-1}) and less hard (0.1581 eV^{-1}) than **TFMOS** (softness: 0.227 eV^{-1} and hardness: 2.193 eV^{-1}). Comparatively, a lower η value and a greater σ value mark the higher potential of **ETPMP** as compared to **MFIP** for NLO applications.

5.4. Natural Population Analysis. The Mulliken charges of the studied crystal chromophores (**ETPMP** and **TFMOS**) are calculated using the same DFT functional.[55] They facilitate in deciding the geometry as well as depicting the electronic, linear, and nonlinear optical properties of compounds under discussion.[50,56] Moreover, the atomic charges of individual atoms also determine the bond polarity and bonding capacity of the entire molecule.[57]

Figure 7 displays the atomic charges of both the compounds, i.e., **ETPMP** and **TFMOS**, where the positively charged atoms lie above the horizontal line and negatively charged atoms are present below the *x* axis. It can be seen in both compounds that atoms like O, N, F, and Cl possess negative values of Mulliken charges. The Mulliken population investigation reveals that no charge discrepancy is observed in the case of H atoms, so most of the hydrogen atoms show positive charges (see Figure 7), whereas an obvious charge difference is seen in the case of C atoms because of the influence of electron-withdrawing atoms surrounding carbons in the structure of both molecules (Figure 7). The C atoms showing negative charges mostly belong to the benzene ring that pertains to unequal distribution of charge density over the entire crystal molecule.[58] Moreover, the C atoms surrounded by more electronegative O atoms become inductively electronegative and hence show negative Mulliken charges. However, a few C atoms neighboring the benzene ring show positive values, among which the last C atom in both compounds shows an extraordinarily higher value of atomic charge as can be seen clearly in Figure 7. Concluding the above discussion, the Mulliken population examination of the molecules offers insight into the phenomena of electronegativity equalization and atomic charge transformation that take place on the external surface of systems during the chemical reaction.[59]

5.5. Natural Bond Orbital (NBO) Analysis. Natural bond orbital (NBO) study is predominant for understanding the intramolecular charge transfer (ICT) between filled and empty orbitals as well as the hyperconjugative interactions.[60−62] The occupied natural bond orbitals are regarded as the Lewis type (donor species), whereas the vacant antibonding orbitals are denoted as non-Lewis type representing the characteristics of

https://doi.org/10.1021/acsomega.3c05199
ACS Omega 2024, 9, 2325−2338

acceptor.[60] The NBO analysis for **ETPMP** and **TFMOS** was performed by using the M06 level in combination with a 6-31G (d,p) basis set. The important parameter in this study is known as stabilization energy, which can be determined by the following eq 8 via using second-order perturbation theory.[63−66]

$$E^{(2)} = q_i \frac{(F_{i,j})^2}{\varepsilon_j - \varepsilon_i} \quad (8)$$

Here, $E^{(2)}$ is the stabilization energy for the given crystal chromophore; the subscripts i and j represent donor and acceptor moieties, respectively; q_i represents the donor orbital occupancy, and $\varepsilon_j - \varepsilon_i$ and $F_{i,j}$ act for diagonal and off-diagonal NBO Fock matrix elements, respectively. The representative values for **ETPMP** and **TFMOS** are tabulated in . Meanwhile, the detailed data for transitions along with their energy values are presented in the Supporting Information (see Tables S4 and S5).

Four types of electronic transitions were commonly observed: $\sigma \rightarrow \sigma^*$, $\pi \rightarrow \pi^*$, LP $\rightarrow \sigma^*$, and LP $\rightarrow \pi^*$. The $\pi \rightarrow \pi^*$ transitions are the most prominent in both the studied chromophores, whereas $\sigma \rightarrow \sigma^*$ transitions are the least dominant. Meanwhile, LP $\rightarrow \sigma^*$ and LP $\rightarrow \pi^*$ are slightly dominant transitions in both compounds. The most significant $\pi \rightarrow \pi^*$ electronic interactions in **ETPMP** and **TFMOS** with maximum stabilization energies are observed to be π(C26−C27) $\rightarrow \pi^*$(C29−C30) and π(N6−C23) $\rightarrow \pi^*$(C8−C21) with stabilization energies as 23.21 and 38.73 kcal mol^{-1}, respectively. Meanwhile, π(C8−C9) $\rightarrow \pi^*$(C8−C9) and (N6−C23) $\rightarrow \pi^*$(N6−C23) are observed with minimum stabilization energies of 1.74 and 1.01 kcal mol^{-1}, respectively. In the case of the **ETPMP** compound, LP2(O4) $\rightarrow \pi^*$(C8−C9) and LP2(F3) $\rightarrow \pi^*$(C29−C30) are the most prominent and feeble transitions with the highest and lowest values of stabilization energies of 39.35 and 0.53 kcal mol^{-1}, respectively. Some significant resonance interactions are also observed in the other crystal, i.e., **TFMOS**, which are LP1(C31) $\rightarrow \pi^*$(N6−C23) and LP1(F1)$\rightarrow \sigma^*$(C26−C33) with stabilization energies of 299.5 and 0.54 kcal mol^{-1}, correspondingly. The feeble electronic transitions are $\sigma \rightarrow \sigma^*$ that occur because of weaker electronic transitions and show some valuable transition energies such as 5.73 and 5.51 observed in σ(O4−H5) $\rightarrow \sigma^*$(C9−C10) and σ(C11−C13) $\rightarrow \sigma^*$(O5−C10), respectively. Meanwhile, σ(C17−C20) $\rightarrow \sigma^*$(C20−H23) and σ(C24−C26) $\rightarrow \sigma^*$(F3−C33) exhibited minimum values for $\sigma \rightarrow \sigma^*$ transitions, i.e., 0.5 and 0.52 kcal mol^{-1} in **ETPMP** and **TFMOS**, respectively.

Hence, the NBO investigation of the studied chromophores provides evidence that prolonged hyperconjugation and strong ICT play a crucial role in stabilizing these systems and provide evidence of charge transfer characteristics that are significant for potential NLO properties.

5.6. UV−Visible Analysis. UV−vis spectroscopy is a fundamental method to study the electronic transition state, probability of charge transfer within the molecule, and contributing configurations of the transitions.[67] The time-dependent density functional theory (TD-DFT) computations were accomplished at the M06 level of theory and the 6-31G(d,p) basis set for exploring the photophysical characteristics of **ETPMP** and **TFMOS**. Furthermore, a brief description of excitation energies (eV), calculated wavelengths (λ_{max}), oscillator strengths (f_{os}), and percentages of major contributions of molecular orbitals (MOs) are shown in Table 6 (Table S10).

Table 6. Transition Energy (E), Maximum Absorption Wavelength (λ_{max}), Oscillator Strength (f_{os}), and Major Transition Contributions of Investigated Molecules (TFMOS and ETPMP) at the M06/6-31G(d,p) Level[a]

parameter	ETPMP	TFMOS
λ_{max} (nm)	305.455	317.225
E (eV)	4.059	3.908
f_{os}	0.474	0.556
MO contributions (%)	H-1 → L (84%)	H-1 → L (95%)

[a]MO = molecular orbital, H = HOMO, L = LUMO.

The theoretically calculated maximum absorption wavelength (λ_{max}) for **ETPMP** is observed at 305.455 nm, which is comparable to its experimentally determined value of λ_{max} (313 nm in the DMSO solvent). This good agreement between theoretically computed and experimentally determined results of maximum absorbance reveals that the selected functional (M06/6-31G(d,p)) is suitable for the current investigation. Interestingly, **TFMOS** displays red-shifted absorption by exhibiting its absorption at 317.225 nm. This bathochromic shift in **TFMOS** might be attributed to the replacement of ethoxy with a methoxy group at the meta position and enhancement of conjugation owing to the substitution of the alcoholic group with a carbonyl functional group in **TFMOS**. Moreover, the oscillator frequency (f_{os}) results are found at 0.474 and 0.556 along with the major transitions (84 and 95% in H-1 → L) for **ETPMP** and **TFMOS**, respectively (see Table 6). In addition to this, the similar compound **TFMOS** showed its absorption at 312 nm accompanied by a 0.572 oscillator strength. Thus, the previously discussed absorption data indicated that compound **TFMOS** displayed a greater value of λ_{max} (317.225 nm) and a lower value of the excitation energy as 0.556 eV.

This discussion suggested that this quantum chemical approach will provide insight into exploring NLO materials with excellent photophysical properties and optical tools with efficient performance to be used in the modern era of high-tech applications.

5.7. Nonlinear Optical Investigation. The revolutionary and growing fields of electro-optic modulation, second-harmonic generation, and more desirable applications related to the era of potential communication led to the invention of substances possessing better NLO characteristics.[68−70] The noncentrosymmetric nature crystals can be efficiently utilized to generate a nonlinear response.[71,72] The modifications in the molecular structures such as positioning of appropriate donor−acceptor moieties instigate NLO response and are the primary function for NLO materials.[67,73,74] The NLO parameters like average linear polarizability response $\langle\alpha\rangle$, electronic dipole moment (μ), and second hyperpolarizability γ_{tot} of investigated chromophores, i.e., **ETPMP** and **TFMOS**, have been computed via the M06 methodology using the 6-31G(d,p) basis set, and the results are displayed in Tables S11 and S12. The values of $\langle\alpha\rangle$ are estimated by the following eq 9.

$$\langle a \rangle = 1/3(\alpha_{xx} + \alpha_{yy} + \alpha_{zz}) \quad (9)$$

The second hyperpolarizabilities ($\gamma_{tot.}$) are calculated by using eq 10.

https://doi.org/10.1021/acsomega.3c05199
ACS Omega 2024, 9, 2325−2338

$$\gamma \text{tot.} = \sqrt{\gamma_x^2 + \gamma_y^2 + \gamma_z^2} \quad (10)$$

where $\gamma_i = \frac{1}{15}\sum_j (\gamma_{ijji} + \gamma_{ijij} + \gamma_{iijj}) i, j = \{x, y, z\}$.

The dipole moment is estimated with the help of eq 11.

$$\mu = (\mu^2{}_x + \mu^2{}_y + \mu^2{}_z)^{1/2} \quad (11)$$

The statistics for dipole moment (μ) confirm that the **TFMOS** compound has greater polarizability than **ETPMP** due to its higher dipole moment (5.777 ⟩ 3.199 D). The tensor along the y axis is dominant in **TFMOS** (5.576 D), whereas in the case of **ETPMP**, μ_x is the major contributing tensor (2.628 D). The variation of NLO parameters like $\langle a \rangle$ and γ_{tot} in the studied donor−acceptor configurations reveal some interesting facts about the synthesized chromophores (**TFMOS** and **ETPMP**) that defend their NLO features excellently. According to the obtained data, the polarizability tensor along the x axis shows a major contribution toward average polarizability $\langle a \rangle$ in **TFMOS** (6.457×10^{-23} esu), whereas the lowest contribution is observed along the z axis (1.308×10^{-23} esu). From the literature survey, it can be inferred that the energy gap between LUMO and HOMO affects the polarizability of a molecule. Mostly, the compounds with lesser band gaps show larger polarizability values. Therefore, the $\langle a \rangle$ value in **TFMOS** is higher than its counterpart **ETPMP** (3.835×10^{-23} ⟩ 3.783×10^{-23} esu) in accordance with its lesser energy gap (3.489 ⟨ 4.300 eV).

The computed data for the second hyperpolarizability (γ_{tot}) also show the major contribution along the x axis, i.e., γ_x, by displaying the highest value in both the studied compounds (1.344×10^{-34} and 8.447×10^{-35} esu) similar to the other NLO parameter $\langle a \rangle$. Moreover, the average value of the third NLO parameter γ_{tot} is found with a higher magnitude in the crystal chromophore **TFMOS** (1.346×10^{-34} esu) as compared to **ETPMP** (8.547×10^{-35} esu). Additionally, the computed values of $\langle a \rangle$ and γ_{tot} of previously reported synthesized compounds of a similar type crystal (**MFIP**) are 3.741×10^{-23} and 1.048×10^{-34} esu, respectively. So, the comparison of our synthesized crystal (**ETPMP**) with **TFMOS** demonstrated the higher results of $\langle a \rangle$ and comparable value of γ_{tot} for **TFMOS**, which illustrated it as a significant NLO material.

6. CONCLUSIONS

Herein, an imine-based Schiff base (**ETPMP**) was synthesized via condensation reaction, and its structure confirmation was done through SC-XRD. The SC-XRD showed that the molecular configuration was stabilized by intramolecular O−H···N bonding and molecular connections were established by C−H···O and C−H···F bonding. Further, Hirshfeld surface analysis also supported XRD as it shows that H···H, H···F, H···C, and H···O were the significant contributors to the stabilization of the supramolecular assembly. The void analysis predicted that **ETPMP** would show a good mechanical response. Interaction energy calculations inferred that the dispersion energy was the most prominent contributor to the supramolecular assembly. Accompanying this, the NLO properties of **ETPMP** and already reported crystal **TFMOS** were investigated through the DFT approach. By correlating the results of FMO analysis with those of GRPs, **TFMOS** demonstrated lower global hardness (0.1281 eV) and greater softness (7.8064 eV^{-1}) because of its smaller energy gap (3.489 eV) and bathochromic shift (317.225 nm). Owing to these particular properties of **TFMOS**, remarkable NLO results, i.e., μ = 5.777 D, $\langle a \rangle = 3.835 \times 10^{-23}$ esu, and $\gamma_{tot.} = 1.346 \times 10^{-34}$ esu, were exhibited by **TFMOS** that illustrated it as an efficient NLO material.

■ ASSOCIATED CONTENT

Supporting Information

The Supporting Information is available free of charge at https://pubs.acs.org/doi/10.1021/acsomega.3c05199.

NBO, UV−vis data (wavelength, excitation energies, and oscillator strengths), FMO and NLO of reported chromophores were calculated using M06/6-31G (d,p) (PDF)

Moreover, crystallographic information is collected of entitled compound (CIF)

■ AUTHOR INFORMATION

Corresponding Authors

Muhammad Adnan Asghar − *Department of Chemistry, Division of Science and Technology, University of Education Lahore, Lahore 54770, Pakistan;* orcid.org/0000-0003-0071-3580; Email: adnan.muhammad@ue.edu.pk

Suvash Chandra Ojha − *Department of Infectious Diseases, The Affiliated Hospital of Southwest Medical University, Luzhou 646000, China*; Email: suvash_ojha@swmu.edu.cn

Authors

Muhammad Nawaz Tahir − *Department of Physics, University of Sargodha, Sargodha 40100, Pakistan*

Muhammad Ashfaq − *Department of Physics, University of Sargodha, Sargodha 40100, Pakistan;* orcid.org/0000-0001-6663-8777

Khurram Shahzad Munawar − *Institute of Chemistry, University of Sargodha, Sargodha 40100, Pakistan; Department of Chemistry, University of Mianwali, Mianwali 42200, Pakistan;* orcid.org/0000-0001-9055-2519

Ahsan Ullah Khan − *Department of Physics, University of Sargodha, Sargodha 40100, Pakistan*

Tansir Ahamad − *Department of Chemistry, College of Science, King Saud University, Riyadh 11451, Saudi Arabia*

Complete contact information is available at: https://pubs.acs.org/10.1021/acsomega.3c05199

Notes

The authors declare no competing financial interest.

■ ACKNOWLEDGMENTS

The authors thank the Researchers Supporting Project number (RSP2024R6), King Saud University, Riyadh, Saudi Arabia. S.C.O. acknowledges the support from the doctoral research fund of the Affiliated Hospital of Southwest Medical University.

■ REFERENCES

(1) Lupaşcu, G.; Pahonţu, E.; Shova, S.; Bărbuceanu, Ş. F.; Ilieş, D. C.; Badea, M.; Paraschivescu, C.; Ducu, C.; Neamţu, J.; Dinu, M.; Ancuceanu, R. V.; Drăgănescu, D.; Dinu-Pîrvu, C. E. Synthesis, Characterization, Crystal Structure and Toxicity Evaluation of Co (II), Cu (II), Mn (II), Ni (II), Pd (II) and Pt (II) Complexes with Schiff Base Derived from 2-chloro-5-(Trifluoromethyl)Aniline. *Appl. Organomet. Chem.* **2020**, *34* (11), No. e5931.

(2) Munawar, K. S.; Haroon, S. M.; Hussain, S. A.; Raza, H. Schiff Bases: Multipurpose Pharmacophores with Extensive Biological Applications. *J. Basic Appl. Sci.* **2018**, *14*, 217−229.
(3) Da Silva, C. M.; da Silva, D. L.; Modolo, L. V.; Alves, R. B.; de Resende, M. A.; Martins, C. V.; de Fátima, Â. Schiff Bases: A Short Review of Their Antimicrobial Activities. *J. Adv. Res.* **2011**, *2* (1), 1−8.
(4) Rauf, A.; Shah, A.; Munawar, K. S.; Khan, A. A.; Abbasi, R.; Yameen, M. A.; Khan, A. M.; Khan, A. R.; Qureshi, I. Z.; Kraatz, H. B.; Zia-ur-Rehman. Synthesis, Spectroscopic Characterization, DFT Optimization and Biological Activities of Schiff Bases and Their Metal (II) Complexes. *J. Mol. Struct.* **2017**, *1145*, 132−140.
(5) Shabbir, M.; Akhter, Z.; Ahmad, I.; Ahmed, S.; Shafiq, M.; Mirza, B.; McKee, V.; Munawar, K. S.; Ashraf, A. R. Schiff Base Triphenylphosphine Palladium (II) Complexes: Synthesis, Structural Elucidation, Electrochemical and Biological Evaluation. *J. Mol. Struct.* **2016**, *1118*, 250−258.
(6) Pervaiz, M.; Ahmad, I.; Yousaf, M.; Kirn, S.; Munawar, A.; Saeed, Z.; Adnan, A.; Gulzar, T.; Kamal, T.; Ahmad, A.; Rashid, A. Synthesis, Spectral and Antimicrobial Studies of Amino Acid Derivative Schiff Base Metal (Co, Mn, Cu, and Cd) Complexes. *Spectrochim. Acta, Part A* **2019**, *206*, 642−649.
(7) Demir Kanmazalp, S.; Doâan, O. E.; Dege, N.; Aâar, E.; Bulbul, H.; Golenya, I. A. (Z)-3-({[3-Methoxy-5-(Trifluoromethyl) Phenyl] Imino} Methyl) Benzene-1, 2-Diol. *Acta Crystallogr. Sect. E Crystallogr. Commun.* **2019**, *75* (4), 470−474.
(8) Munawar, K. S.; Ali, S.; Tahir, M. N.; Khalid, N.; Abbas, Q.; Qureshi, I. Z.; Shahzadi, S. Investigation of Derivatized Schiff Base Ligands of 1, 2, 4-Triazole Amine and Their Oxovanadium (IV) Complexes: Synthesis, Structure, DNA Binding, Alkaline Phosphatase Inhibition, Biological Screening, and Insulin Mimetic Properties. *Russ. J. Gen. Chem.* **2015**, *85*, 2183−2197.
(9) Kargar, H.; Fallah-Mehrjardi, M.; Behjatmanesh-Ardakani, R.; Munawar, K. S.; Ashfaq, M.; Tahir, M. N. Titanium (IV) Complex Containing ONO-Tridentate Schiff Base Ligand: Synthesis, Crystal Structure Determination, Hirshfeld Surface Analysis, Spectral Characterization, Theoretical and Computational Studies. *J. Mol. Struct.* **2021**, *1241*, No. 130653.
(10) Shi, L.; Ge, H.-M.; Tan, S.-H.; Li, H.-Q.; Song, Y.-C.; Zhu, H.-L.; Tan, R.-X. Synthesis and Antimicrobial Activities of Schiff Bases Derived from 5-Chloro-Salicylaldehyde. *Eur. J. Med. Chem.* **2007**, *42* (4), 558−564.
(11) Welch, J. T.; Eswaraskrishnan, S. *Fluorine in Bioorganic Chemistry*. Wiley 1991.
(12) Yildiz, M. Synthesis and Spectroscopic Studies of Some New Polyether Ligands of the Schiff Base Type. *Spectrosc. Lett.* **2004**, *37* (4), 367−381.
(13) Kargar, H.; Nateghi-Jahromi, M.; Fallah-Mehrjardi, M.; Behjatmanesh-Ardakani, R.; Munawar, K. S.; Ali, S.; Ashfaq, M.; Tahir, M. N. Synthesis, Spectral Characterization, Crystal Structure and Catalytic Activity of a Novel Dioxomolybdenum Schiff Base Complex Containing 4-Aminobenzhydrazone Ligand: A Combined Experimental and Theoretical Study. *J. Mol. Struct.* **2022**, *1249*, No. 131645.
(14) Yıldız, M.; Karpuz, Ö.; Zeyrek, C. T.; Boyacıoğlu, B.; Dal, H.; Demir, N.; Yıldırım, N.; Ünver, H. Synthesis, Biological Activity, DNA Binding and Anion Sensors, Molecular Structure and Quantum Chemical Studies of a Novel Bidentate Schiff Base Derived from 3, 5-Bis (Triflouromethyl) Aniline and Salicylaldehyde. *J. Mol. Struct.* **2015**, *1094*, 148−160.
(15) Shahzad Munawar, K.; Ali, S.; Ashfaq, M.; Nawaz Tahir, M.; Muhammad, S.; Alarfaji, S. S.; Ahmed, G.; Al-Sehemi, A. G. Synthesis, Characterization, Crystal Structure and Computational Study of Third-Order NLO Properties of Schiff Bases. *ChemistrySelect* **2022**, *7* (43), No. e202203015.
(16) Karakas, A.; Unver, H.; Elmali, A. THE INVESTIGATION OF ELECTRONIC PROPERTIES AND MICROSCOPIC SECOND-ORDER NONLINEAR OPTICAL BEHAVIOR OF 1-SALICYLIDENE-3-THIO-SEMICARBAZONE. *J. Nonlinear Opt. Phys. Mater.* **2007**, *16* (01), 91−99.
(17) Munawar, K. S.; Ali, S.; Rauf, A.; Bibi, S.; Ashfaq, M.; Tahir, M. N.; urRehman, S.; Rasool, L. Structural and Computational Analysis, Spectroscopic and Electrochemical Elucidation of a Schiff Base. *J. Iran. Chem. Soc.* **2022**, *19* (9), 3845−3860.
(18) Ashfaq, M.; Khalid, M.; Tahir, M. N.; Ali, A.; Arshad, M. N.; Asiri, A. M. Synthesis of Crystalline Fluoro-Functionalized Imines, Single Crystal Investigation, Hirshfeld Surface Analysis, and Theoretical Exploration. *ACS Omega* **2022**, *7* (11), 9867−9878.
(19) Sheldrick, G. M. SHELXT−Integrated Space-Group and Crystal-Structure Determination. *Acta Crystallogr. Sect. Found. Adv.* **2015**, *71* (1), 3−8.
(20) Sheldrick, G. M. Crystal Structure Refinement with SHELXL. *Acta Crystallogr. Sect. C Struct. Chem.* **2015**, *71* (1), 3−8.
(21) Farrugia, L. J. WinGX and ORTEP for Windows: An Update. *J. Appl. Crystallogr.* **2012**, *45* (4), 849−854.
(22) Spek, A. L. Structure Validation in Chemical Crystallography. *Acta Crystallogr. D Biol. Crystallogr.* **2009**, *65* (2), 148−155.
(23) Wang, Y.; Verma, P.; Jin, X.; Truhlar, D. G.; He, X. Revised M06 Density Functional for Main-Group and Transition-Metal Chemistry. *Proc. Natl. Acad. Sci. U. S. A.* **2018**, *115* (41), 10257−10262.
(24) Martins, L. S. C.; Jorge, F. E.; Franco, M. L.; Ferreira, I. B. All-Electron Gaussian Basis Sets of Double Zeta Quality for the Actinides. *J. Chem. Phys.* **2016**, *145* (24), 244113 DOI: 10.1063/1.4973377.
(25) Frisch, A.; Nielson, A. B.; Holder, A. J. *Gaussview User Manual*. Gaussian Inc: Pittsburgh PA,2000, *556*.
(26) O'boyle, N. M.; Tenderholt, A. L.; Langner, K. M. Cclib: A Library for Package-independent Computational Chemistry Algorithms. *J. Comput. Chem.* **2008**, *29* (5), 839−845.
(27) Hanwell, M. D.; Curtis, D. E.; Lonie, D. C.; Vandermeersch, T.; Zurek, E.; Hutchison, G. R. Avogadro: An Advanced Semantic Chemical Editor, Visualization, and Analysis Platform. *J. Cheminformatics* **2012**, *4* (1), 17.
(28) Zhurko, G. A. *Chemcraft*: Http://Www.Chemcraftprog.Com. Receiv. Oct. **2014**, *22*.
(29) Lu, T.; Chen, F. Multiwfn: A Multifunctional Wavefunction Analyzer. *J. Comput. Chem.* **2012**, *33* (5), 580−592.
(30) Padhiary, A.; Mir, S. A.; Tete, S. S.; Baitharu, I.; Nayak, B. Identification of Anti-Cyanobacterial Leads Targeting Carbonic Anhydrase from Phytochemical Database Using in Silico Approach. *Biotechnologia* **2023**, *104* (2), 121.
(31) Weinhold, F.; Glendening, E. D. *NBO 5.0 Program Manual: Natural Bond Orbital Analysis Programs*. Theoretical Chemistry Institute and Department of Chemistry University of Wisconsin: Madison WI **2001**, *53706*.
(32) Bernstein, J.; Davis, R. E.; Shimoni, L.; Chang, N. Patterns in Hydrogen Bonding: Functionality and Graph Set Analysis in Crystals. *Angew. Chem., Int. Ed. Engl.* **1995**, *34* (15), 1555−1573.
(33) Groom, C. R.; Bruno, I. J.; Lightfoot, M. P.; Ward, S. C. The Cambridge Structural Database. *Acta Crystallogr. Sect. B Struct. Sci. Cryst. Eng. Mater.* **2016**, *72* (2), 171−179.
(34) Shuja, S.; Ali, S.; Meetsma, A.; Broker, G. A.; Tiekink, E. R. 3-[3-(Trifluoromethyl) Phenyliminomethyl] Benzene-1, 2-Diol. *Acta Crystallogr. Sect. E Struct. Rep. Online* **2007**, *63* (4), o1781−o1782.
(35) Akkaya, A.; Erşahin, F.; Ağar, E.; Şenel, İ.; Büyükgüngör, O. (E)-2-Methyl-6-[3-(Trifluoromethyl) Phenyliminomethyl] Phenol. *Acta Crystallogr. Sect. E Struct. Rep. Online* **2007**, *63* (8), o3555−o3555.
(36) Hajam, T. A.; Saleem, H.; Oadhusha, M. S. A.; Ameen, K. K. M. Synthesis, quantum chemical calculations and molecular docking studies of 2-ethoxy-4[(2-trifluromethyl-phenylimino)methyl]phenol. *Mol. Phys.* **2020**, *118* (24), No. e1781945, DOI: 10.1080/00268976.2020.1781945.
(37) Spackman, P. R.; Turner, M. J.; McKinnon, J. J.; Wolff, S. K.; Grimwood, D. J.; Jayatilaka, D.; Spackman, M. A. CrystalExplorer: A Program for Hirshfeld Surface Analysis, Visualization and Quantita-

https://doi.org/10.1021/acsomega.3c05199
ACS Omega 2024, 9, 2325−2338

tive Analysis of Molecular Crystals. *J. Appl. Crystallogr.* **2021**, *54* (3), 1006−1011.
(38) Spackman, M. A.; Jayatilaka, D. Hirshfeld Surface Analysis. *CrystEngComm* **2009**, *11* (1), 19−32.
(39) Turner, M. J.; McKinnon, J. J.; Jayatilaka, D.; Spackman, M. A. Visualisation and Characterisation of Voids in Crystalline Materials. *CrystEngComm* **2011**, *13* (6), 1804−1813.
(40) Shafiq, I.; Khalid, M.; Asghar, M. A.; Adeel, M.; ur Rehman, M. F.; Syed, A.; Bahkali, A. H.; Elgorban, A. M.; Akram, M. S. Exploration of Photovoltaic Behavior of Benzodithiophene Based Non-Fullerene Chromophores: First Theoretical Framework for Highly Efficient Photovoltaic Parameters. *J. Mater. Res. Technol.* **2023**, *24*, 1882−1896.
(41) Dege, N.; Gökce, H.; Doğan, O. E.; Alpaslan, G.; Ağar, T.; Muthu, S.; Sert, Y. Quantum Computational, Spectroscopic Investigations on N-(2-((2-Chloro-4,5-Dicyanophenyl)Amino)-Ethyl)-4-Methylbenzenesulfonamide by DFT/TD-DFT with Different Solvents, Molecular Docking and Drug-Likeness Researches. *Colloids Surf. Physicochem. Eng. Asp.* **2022**, *638*, No. 128311.
(42) Karrouchi, K.; Brandón, S. A.; Sert, Y.; El-marzouqi, H.; Radi, S.; Ferbinteanu, M.; Faouzi, M. E. A.; Garcia, Y.; Ansar, M. Synthesis, X-Ray Structure, Vibrational Spectroscopy, DFT, Biological Evaluation and Molecular Docking Studies of (E)-N'-(4-(Dimethylamino) Benzylidene)-5-Methyl-1H-Pyrazole-3-Carbohydrazide. *J. Mol. Struct.* **2020**, *1219*, No. 128541.
(43) Sert, Y.; Gümüş, M.; Gökce, H.; Kani, İ.; Koca, İ. Molecular Docking, Hirshfeld Surface, Structural, Spectroscopic, Electronic, NLO and Thermodynamic Analyses on Novel Hybrid Compounds Containing Pyrazole and Coumarin Cores. *J. Mol. Struct.* **2018**, *1171*, 850−866.
(44) Abdulridha, A. A.; Allah, M. A. A. H.; Makki, S. Q.; Sert, Y.; Salman, H. E.; Balakit, A. A. Corrosion inhibition of carbon steel in 1 M H2SO4 using new Azo Schiff compound: Electrochemical, gravimetric, adsorption, surface and DFT studies. *J. Mol. Liq.* **2020**, *315*, No. 113690.
(45) Albo Hay Allah, M. A.; Balakit, A. A.; Salman, H. I.; Abdulridha, A. A.; Sert, Y. New Heterocyclic Compound as Carbon Steel Corrosion Inhibitor in 1 M H_2SO_4, High Efficiency at Low Concentration: Experimental and Theoretical Studies. *J. Adhes. Sci. Technol.* **2023**, *37* (3), 525−547.
(46) Pearson, R. G. Absolute Electronegativity and Absolute Hardness of Lewis Acids and Bases. *J. Am. Chem. Soc.* **1985**, *107* (24), 6801−6806.
(47) Parr, R. G.; Yang, W. Density Functional Approach to the Frontier-Electron Theory of Chemical Reactivity. *J. Am. Chem. Soc.* **1984**, *106* (14), 4049−4050.
(48) Parr, R. G.; Donnelly, R. A.; Levy, M.; Palke, W. E. Electronegativity: The Density Functional Viewpoint. *J. Chem. Phys.* **1978**, *68* (8), 3801−3807.
(49) Politzer, P.; Truhlar, D. G. *Chemical Applications of Atomic and Molecular Electrostatic Potentials: Reactivity, Structure, Scattering, and Energetics of Organic, Inorganic, and Biological Systems*; Springer Science & Business Media: New York, NY 2013 DOI: 10.1007/978-1-4757-9634-6.
(50) Parr, R. G.; Pearson, R. G. Absolute Hardness: Companion Parameter to Absolute Electronegativity. *J. Am. Chem. Soc.* **1983**, *105* (26), 7512−7516.
(51) Parthasarathi, R.; Padmanabhan, J.; Elango, M.; Subramanian, V.; Chattaraj, P. K. Intermolecular Reactivity through the Generalized Philicity Concept. *Chem. Phys. Lett.* **2004**, *394* (4−6), 225−230.
(52) Savchenko, R. G.; Mescheryakova, E. S.; Bikmukhametov, K. S.; Tulyabaev, A. R.; Parfenova, L. V.; Khalilov, L. M. Hydroxy Derivatives of Poststerone and Its Nontrivial 13 (14→ 8)-Abeo-Analogues: Synthesis, Crystal Packing, and Intermolecular Hydrogen Bonds. *J. Mol. Struct.* **2021**, *1227*, No. 129509.
(53) Tsuneda, T.; Song, J.-W.; Suzuki, S.; Hirao, K. On Koopmans' Theorem in Density Functional Theory. *J. Chem. Phys.* **2010**, *133* (17), 174101 DOI: 10.1063/1.3491272.
(54) Koopmans, T. Über Die Zuordnung von Wellenfunktionen Und Eigenwerten Zu Den Einzelnen Elektronen Eines Atoms. *physica* **1934**, *1* (1−6), 104−113.
(55) Khalid, M.; Shafiq, I.; Zhu, M.; Khan, M. U.; Shafiq, Z.; Iqbal, J.; Alam, M. M.; Braga, A. A. C.; Imran, M. Efficient Tuning of Small Acceptor Chromophores with A1-π-A2-π-A1 Configuration for High Efficacy of Organic Solar Cells via End Group Manipulation. *J. Saudi Chem. Soc.* **2021**, *25* (8), No. 101305.
(56) Khalid, M.; Shafiq, I.; Umm-e-Hani; Mahmood, K.; Hussain, R.; Ur Rehman, M. F.; Assiri, M. A.; Imran, M.; Akram, M. S. Effect of Different End-Capped Donor Moieties on Non-Fullerenes Based Non-Covalently Fused-Ring Derivatives for Achieving High-Performance NLO Properties. *Sci. Rep.* **2023**, *13* (1), 1395.
(57) Burrows, J.; Pauling, A. Linus. The Nature of the Chemical Bond and the Structure of Molecules Aid Crystals. Ithaca: The Cornell University Press, 1939. 430 p. $4.50. *Sci. Educ.* **1941**, *25* (2), 120.
(58) Li, L.; Wu, C.; Wang, Z.; Zhao, L.; Li, Z.; Sun, C.; Sun, T. Density Functional Theory (DFT) and Natural Bond Orbital (NBO) Study of Vibrational Spectra and Intramolecular Hydrogen Bond Interaction of l-Ornithine−l-Aspartate. *Spectrochim. Acta. A. Mol. Biomol. Spectrosc.* **2015**, *136*, 338−346.
(59) Mulliken, R. S. Electronic Population Analysis on LCAO−MO Molecular Wave Functions I. *J. Chem. Phys.* **1955**, *23* (10), 1833−1840.
(60) Szafran, M.; Komasa, A.; Bartoszak-Adamska, E. Crystal and Molecular Structure of 4-Carboxypiperidinium Chloride (4-Piperidinecarboxylic Acid Hydrochloride). *J. Mol. Struct.* **2007**, *827* (1−3), 101−107.
(61) Khalid, M.; Khan, M. U.; Shafiq, I.; Hussain, R.; Mahmood, K.; Hussain, A.; Jawaria, R.; Hussain, A.; Imran, M.; Assiri, M. A.; Ali, A.; ur Rehman, M. F.; Sun, K.; Li, Y. NLO Potential Exploration for D−π−A Heterocyclic Organic Compounds by Incorporation of Various π-Linkers and Acceptor Units. *Arab. J. Chem.* **2021**, *14* (8), No. 103295.
(62) Khalid, M.; Ali, A.; Asim, S.; Tahir, M. N.; Khan, M. U.; Vieira, L. C. C.; de la Torre, A. F.; Usman, M. Persistent Prevalence of Supramolecular Architectures of Novel Ultrasonically Synthesized Hydrazones Due to Hydrogen Bonding [X−H··· O; X= N]: Experimental and Density Functional Theory Analyses. *J. Phys. Chem. Solids* **2021**, *148*, No. 109679.
(63) Krishnan, K. G.; Sivakumar, R.; Thanikachalam, V.; Saleem, H. Synthesis, Spectroscopic Investigation and Computational Study of 3-(1-(((Methoxycarbonyl) Oxy) Imino) Ethyl)-2H-Chromen-2-One. *Spectrochim. Acta, Part A* **2015**, *144*, 29−42.
(64) Khalid, M.; Arshad, M. N.; Tahir, M. N.; Asiri, A. M.; Naseer, M. M.; Ishaq, M.; Khan, M. U.; Shafiq, Z. An Efficient Synthesis, Structural (SC-XRD) and Spectroscopic (FTIR, 1HNMR, MS Spectroscopic) Characterization of Novel Benzofuran-Based Hydrazones: An Experimental and Theoretical Studies. *J. Mol. Struct.* **2020**, *1216*, No. 128318.
(65) Khalid, M.; Ali, A.; De La Torre, A. F.; Marrugo, K. P.; Concepcion, O.; Kamal, G. M.; Muhammad, S.; Al-Sehemi, A. G. Facile Synthesis, Spectral (IR, Mass, UV−Vis, NMR), Linear and Nonlinear Investigation of the Novel Phosphonate Compounds: A Combined Experimental and Simulation Study. *ChemistrySelect* **2020**, *5* (10), 2994−3006.
(66) Khalid, M.; Larachi, F.; Adnot, A. The Role of Silver Minerals on the Cyanidation of Gold Particles Embedded within Multi-sulphidic Mineral Matrices. *Can. J. Chem. Eng.* **2018**, *96* (10), 2299−2307.
(67) Khan, M. U.; Khalid, M.; Ibrahim, M.; Braga, A. A. C.; Safdar, M.; Al-Saadi, A. A.; Janjua, M. R. S. A. First Theoretical Framework of Triphenylamine−Dicyanovinylene-Based Nonlinear Optical Dyes: Structural Modification of π-Linkers. *J. Phys. Chem. C* **2018**, *122* (7), 4009−4018.
(68) Peng, Z.; Yu, L. Second-Order Nonlinear Optical Polyimide with High-Temperature Stability. *Macromolecules* **1994**, *27* (9), 2638−2640.

(69) Tsutsumi, N.; Morishima, M.; Sakai, W. Nonlinear Optical (NLO) Polymers. 3. NLO Polyimide with Dipole Moments Aligned Transverse to the Imide Linkage. *Macromolecules* **1998**, *31* (22), 7764−7769.
(70) Breitung, E. M.; Shu, C.-F.; McMahon, R. J. Thiazole and Thiophene Analogues of Donor−Acceptor Stilbenes: Molecular Hyperpolarizabilities and Structure−Property Relationships. *J. Am. Chem. Soc.* **2000**, *122* (6), 1154−1160.
(71) Haroon, M.; Khalid, M.; Akhtar, T.; Tahir, M. N.; Khan, M. U.; Saleem, M.; Jawaria, R. Synthesis, Spectroscopic, SC-XRD Characterizations and DFT Based Studies of Ethyl2-(Substituted-(2-Benzylidenehydrazinyl)) Thiazole-4-Carboxylate Derivatives. *J. Mol. Struct.* **2019**, *1187*, 164−171.
(72) Khalid, M.; Naseer, S.; Tahir, M. S.; shafiq, I.; Munawar, K. S.; de Alacntara Morais, S. F.; Braga, A. A. C. A Theoretical Approach towards Designing of Banana Shaped Non-Fullerene Chromophores Using Efficient Acceptors Moieties: Exploration of Their NLO Response Properties. *Opt. Quantum Electron.* **2023**, *55* (3), 258.
(73) Khan, M. U.; Ibrahim, M.; Khalid, M.; Braga, A. A. C.; Ahmed, S.; Sultan, A. Prediction of Second-Order Nonlinear Optical Properties of D−π−A Compounds Containing Novel Fluorene Derivatives: A Promising Route to Giant Hyperpolarizabilities. *J. Clust. Sci.* **2019**, *30*, 415−430.
(74) Khan, M. U.; Ibrahim, M.; Khalid, M.; Jamil, S.; Al-Saadi, A. A.; Janjua, M. R. S. A. Quantum Chemical Designing of Indolo [3, 2, 1-Jk] Carbazole-Based Dyes for Highly Efficient Nonlinear Optical Properties. *Chem. Phys. Lett.* **2019**, *719*, 59−66.

https://doi.org/10.1021/acsomega.3c05199
ACS Omega 2024, 9, 2325−2338